J Solid State Electrochem (2008) 12:1619–1627
DOI 10.1007/s10008-008-0538-y

ORIGINAL PAPER

Synthesis and characterization of submicron size particles of $LiMn_2O_4$ by microemulsion route

Nupur Nikkan Sinha · N. Munichandraiah

Received: 5 December 2007 / Revised: 13 February 2008 / Accepted: 20 February 2008 / Published online: 20 March 2008

Abstract Among the various positive electrode materials investigated for Li-ion batteries, spinel $LiMn_2O_4$ is one of the most important materials. Small particles of the active materials facilitate high-rate capability due to large surface to mass ratio and small diffusion path length. The present work involves the synthesis of submicron size particles of $LiMn_2O_4$ in a quaternary microemulsion medium. The precursor obtained from the reaction is heated at different temperatures in the range from 400 to 900 °C. The samples heated at 800 and 900 °C are found to possess pure spinel phase with particle size <200 nm, as evidenced from XRD, SEM, and TEM studies. The electrochemical characterization studies provide discharge capacity values of about 100 mAh g^{-1} at C/5 rate, and there is a moderate decrease in capacity by increasing the rate of charge–discharge cycling. Studies also include charge–discharge cycling and ac impedance studies in temperature range from −10 to 40 °C. Impedance data are analyzed with the help of an equivalent circuit and a nonlinear least squares fitting program. From temperature dependence of charge-transfer resistance, a value of 0.62 eV is obtained for the activation energy of Mn^{3+}/Mn^{4+} redox process, which accompanies the intercalation/deintercalation of the Li^+ ion in $LiMn_2O_4$.

Keywords $LiMn_2O_4$ cathode material · Microemulsion · Cyclic voltammetry · Charge–discharge cycling · ac impedance

N. N. Sinha · N. Munichandraiah (✉)
Department of Inorganic and Physical Chemistry,
Indian Institute of Science,
Bangalore 560 012, India
e-mail: muni@ipc.iisc.ernet.in

Introduction

Lithium-ion batteries have revolutionized as power sources for portable electronic devices in recent years because of their high working voltage, high energy density, and good cyclability [1]. Usually, the cathode materials of Li-ion batteries are based on a family of lithiated transition metal oxides such as $LiCoO_2$, $LiNiO_2$, $LiMn_2O_4$, etc. [2]. Among these compounds, spinel $LiMn_2O_4$ is interesting as it is inexpensive, environmentally safe, and has a high reduction potential [3]. Electrochemical characteristics of the cathode materials depend on factors such as particle size, surface morphology, homogeneity, etc. [4–6]. Also, it is now well understood that the cathode materials, which consist of particles in nanodimensions, exhibit better characteristics such as high-rate capability, long cycle life, etc. due to larger surface to mass ratio and lower lithium-ion diffusion length in comparison with micron-sized particles [7–9].

Investigations on novel and convenient routes of synthesizing $LiMn_2O_4$ as submicron- or nanometer-sized particles for improved characteristics have become important in recent years. Nanoparticles of spinel $LiMn_2O_4$ are synthesized by a variety of procedures, which include sol–gel [10–14], laser ablation [15], template synthesis [16–18], combustion [19], spray pyrolysis [20, 21], Pechini [22, 23], use of NaCl flux [24], etc. Synthesis of nanoparticles in microemulsion media is a versatile route [25]. This route is employed for the synthesis of $LiMn_2O_4$ to a limited extent [26–29]. Hwang et al. [26] prepared $LiMn_2O_4$ by dissolving stoichiometric quantities of Li_2CO_3 and $Mn(NO_3)_2{\cdot}6H_2O$ in dilute HNO_3 and transferred into a mixture of emulsifying agent and oil. Kerosene and Tween 85 were used as the oil and emulsifying agent, respectively. After storing for a few hours, the emulsion was added dropwise to kerosene at 200 °C and a precursor powder was obtained. The powder

was heated at different temperatures from 400 to 900 °C for several hours to arrive at an optimum condition for the formation of submicron-sized particles of $LiMn_2O_4$. A similar procedure was employed by Myung and Chung [27], but using $LiOH{\cdot}H_2O$, $LiNO_3$, and $Mn(NO_3)_2$ as the starting materials. The size of the $LiMn_2O_4$ particles was <1 μm. Lu and coworkers [28, 29] also employed kerosene as the oil phase and sorbitan monooleate as the emulsion stabilizer. The $LiMn_2O_4$ precursor was obtained by dropping the emulsion consisting of reactants into hot kerosene. The precursor was calcined at elevated temperature. The particle size of $LiMn_2O_4$ then obtained was in the range from 0.1 to 0.4 μm. In all these studies, kerosene was used as the oil and the precursor powders were obtained from kerosene maintained at a temperature as high as 200 °C. This procedure involving kerosene at high temperature appears to be quite cumbersome, and simpler procedures of synthesis in microemulsion media at lower temperatures are preferable. Furthermore, the properties of the reaction products also depend on the nature and the composition of microemulsion.

The aim of the present study is to synthesize the $LiMn_2O_4$ precursor in a quaternary microemulsion at a low temperature without employing kerosene. Cyclohexane is used as the oil in an aqueous solution, the latter being the minor component. Sodium dodecyl sulfate (SDS) and *n*-butanol are used as surfactant and cosurfactant, respectively. Submicron-sized particles of $LiMn_2O_4$, which are obtained after heating the precursor, is subjected to physiochemical and electrochemical characterization studies. Furthermore, the activation energy for the Mn^{3+}/Mn^{4+} redox process, which accompanies the intercalation/deintercalation the of Li^+ ion in $LiMn_2O_4$, is evaluated.

Materials and methods

Analytical grade reagents, namely, lithium acetate (Aldrich), manganese acetate (Spectrochem), cyclohexane (Merck), high-purity SDS (Merck), and *n*-butanol (SD Fine Chemicals) were used for the experiments. Solutions were prepared using doubly distilled water with molar ratio of Li/Mn=1:2. $LiMn_2O_4$ was synthesized from quaternary microemulsion consisting of water, cyclohexane, SDS, and *n*-butanol. A solution was prepared by mixing 51.2 ml cyclohexane (oil), 6.2 ml of *n*-butanol (cosurfactant), and 0.225 g of SDS (surfactant) and stirred well until it became optically transparent. To this nonaqueous medium, 10 ml aqueous solution of 1 M $Mn(CH_3COO)_2$ and 10 ml aqueous solution of 0.5 M CH_3COOLi were added. The emulsion medium was stirred for 12 h followed by evaporation at 120 °C to obtain a brown gel. The gel was heated at 400 °C in air for 6 h and the $LiMn_2O_4$ precursor was obtained. The quantity of the precursor obtained in a batch of synthesis was about 0.450g. Subsequently, the precursor samples were heated at different temperatures ranging from 500 to 900 °C for 6 h to get $LiMn_2O_4$.

For electrochemical characterization, electrodes were prepared on aluminum foil (0.2 mm thick) as a current collector. A foil with an area of 1 cm^2 with tag for electrical connection was polished with successive grades of emery, cleaned with detergent, washed with doubly distilled water, rinsed with acetone, dried, and weighed. $LiMn_2O_4$ (70 wt %), acetylene black (25 wt%), and PVDF (5 wt%) were ground in a motor; a few drops of 1-methyl-2-pyrrolidinone (NMP) were added to get a syrup. It was coated onto a pretreated Al foil (area 1 cm^2) and dried. The coating and drying steps were repeated to get the required loading level (4–6 mg) of the active material. Finally, the electrodes were dried at 110 °C under vacuum for 12 h. The electrochemical cells were assembled in glass containers, using a Li (Aldrich) foil for both the counter and reference electrodes. A microporous polypropylene (Celgard 2400) film was used as the separator. The electrolyte was 1 M $LiAsF_6$ in 1:1 mixed solvents of ethylene carbonate (EC) and dimethyl carbonate (DMC) (all Aldrich). The solvents were repeatedly treated with molecular sieves (4 Å) before preparing the electrolyte. Cells were assembled in an argon atmosphere glove box (MBraun model UNILAB). All potential values are reported against the Li/Li^+ reference electrode.

Powder X-ray diffraction (XRD) patterns were recorded using Philips XRD X'PERT PRO diffractometer using CuK_α (λ=1.5418 Å) as the source. Thermogravimetric analysis (TGA) and differential thermal analysis (DTA) data were recorded in the temperature range from ambient to 900 °C at a heating rate of 10 °C/min in air using a Perkin-Elmer thermal analyzer model Pyris Diamond TG/DTA. Microstructure was examined by the FEI scanning electron microscope model SIRION and FEI high-resolution transition electron microscope (HRTEM) model TECNAI F30.

Cyclic voltammograms were recorded with an EG&G potentiostat model Versastat. The impedance spectra were recorded potentiostatically at open circuit potential with an ac excitation signal of 5 mV (peak to peak) over the frequency range from 100 kHz to 0.01 Hz using Eco Chemie potentiostat/galvanostat model Autolab 30. Impedance data were subjected to nonlinear least squares (NLLS) fitting procedure. Constant current charge–discharge cycling of the electrode was performed using either an Eco Chemie computer-controlled potentiostat/galvanostat model Autolab 30 or a manual galvanostatic circuit consisting of a dc-regulated power supply, a high resistance and an ammeter in series with the cell. A digital multimeter of high-input impedance was employed for measuring electrode potentials. For conducting the experiment in the temperature range

from −10 to 40 °C, a Julabo refrigerator cum heater Model F25 with ethanol as the thermal medium, was employed. At each desired temperature, the cell was equilibrated for 3 h before measurements. The ambient temperature experiments were carried out at 20±1 °C in an air-conditioned room.

Results and discussion

Synthesis

The inverse microemulsion route is a versatile method for the synthesis of a variety of nanomaterials [30]. In this procedure, the reactants are allowed to combine in micrometer- or submicrometer-sized drops of the aqueous phase, which are dispersed in a large volume of the organic phase. As the growth of the reaction product is limited by the size of the aqueous droplets in these nanoreactors [30], the particle size obtained is in submicrometer or nanometer scale. Experimental variables, which influence the particle size of the reaction product, include the concentration of the reactants, relative ratio of the concentration of the reactants, droplet size, adsorption of the surfactant on particles, nature of the cosurfactant, etc. In the present synthesis, 20 ml of the aqueous solution of $Mn(CH_3COO)_2$ and CH_3COOLi was dispersed in 51.2 ml of the organic phase. The aqueous droplets were stabilized by SDS molecules with their polar head groups oriented toward the aqueous drops and the aliphatic tails toward the organic phase. Intermixing of the reactants took place within the droplets. Slow evaporation of the emulsion resulted in the formation of a gel consisting of acetates of Mn and Li in narrow regions, which were surrounded by surfactant molecules. During the subsequent heat treatment, the mixed acetates and the surfactant were oxidized resulting in the formation of submicron-sized particles of $LiMn_2O_4$.

The effect of heating

Thermal analysis data of the precursor sample is shown in Fig. 1. From the TGA trace, there is about 2.5% weight loss when the sample is heated up to 200 °C, which is due to the adsorbed water. Between 200 and 350 °C, about 5.5% weight loss is due to the removal of acetates, which is followed by 2 wt% loss due to the removal of the surfactant. The two exothermic peaks in DTA trace at 130 and 820 °C, respectively, are attributed to the removal of organic parts of the reactants and sodium of the SDS surfactant. The emulsion-derived precursor was dried at different temperatures between 400 and 900 °C. The XRD patterns of the product samples are shown in Fig. 2. It is known that $LiMn_2O_4$ crystallizes in cubic spinel structure with the space group Fd3m. For the sample obtained at

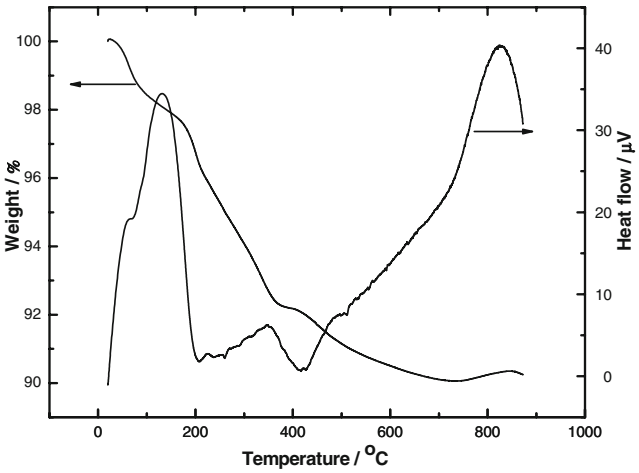

Fig. 1 TGA and DTA curves of precursor $LiMn_2O_4$ recorded at a heating rate of 10 °C min^{-1}

400 °C, prominent peaks corresponding to $LiMn_2O_4$ are observed. However, there are also minor peaks at 2θ=22°, 24°, and 32°, which correspond to Mn_2O_3 as an impurity. As the calcination temperature increases, the impurity peaks decrease and finally disappear at 800 °C. The XRD patterns of the samples obtained at 800 and 900 °C agree with the pattern of the pure cubic spinel phase of $LiMn_2O_4$ (JCPDS file no. 35-782). The main diffraction peaks, namely, (111), (311), and (400) remain at the same 2θ values for all samples. The ratio of the (111) and (311) (or (400)) peaks are greater than unity. The values of lattice parameter a= 8.201 and 8.239 Å, respectively, obtained for the samples

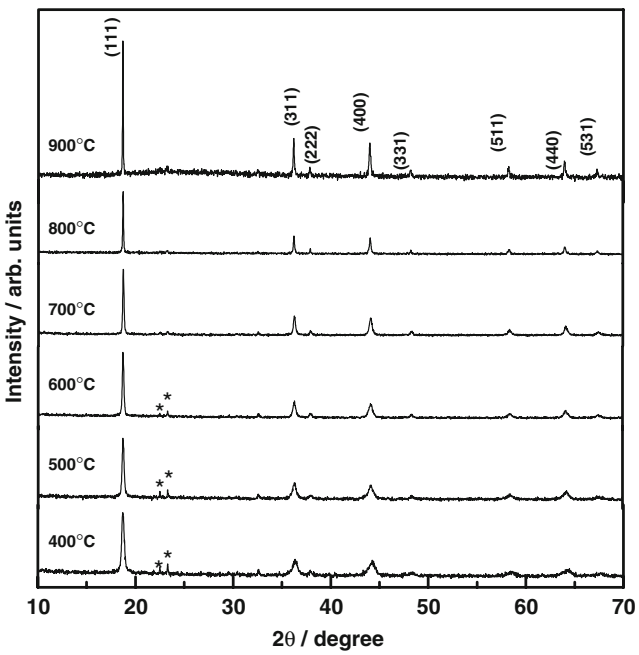

Fig. 2 Powder XRD patterns of $LiMn_2O_4$ samples obtained by heating the precursor at different temperatures. Some impurity peaks are indicated as *asterisks*

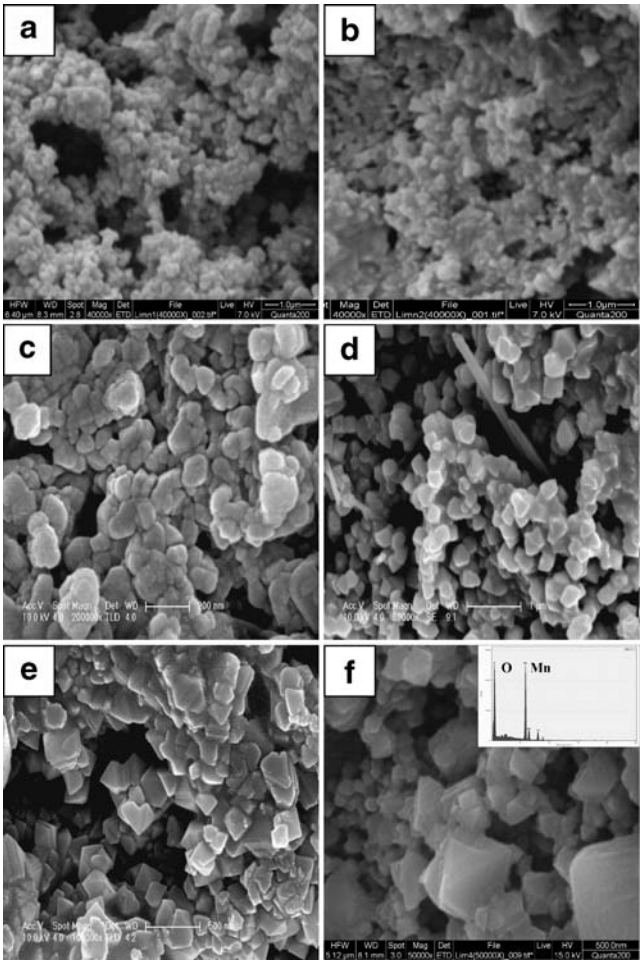

Fig. 3 SEM images of $LiMn_2O_4$ powder by heating the precursors at 400 (**a**), 500 (**b**) 600 (**c**), 700 (**d**), 800 (**e**), and 900 °C (**f**). EDAX data are shown as *inset* in **f**

heated at 800 and 900 °C agree well with the values reported in the literature [31]. It is known that the values of the lattice parameter of $LiMn_2O_4$ powders depend on the heating temperature of the precursor materials. For instance, Naghash and Lee synthesized $LiMn_2O_4$ by aqueous coprecipitation of Li and Mn salts [32]. The precipitate obtained at ambient conditions was calcined at different temperatures and the evolution of the spinel structure was monitored by XRD studies. The lattice parameter increased with the increase of temperature from 8.17 Å at 250 °C to 8.26 Å at 850 °C. In a similar study, Han and Kim synthesized $LiMn_2O_4$ by a modified Pechini method [33]. The precursor samples were calcined at different temperatures between 600 and 800 °C. In this study also, the lattice parameter was found to increase with increasing temperature from 8.230 Å at 600 °C to 8.242 Å at 800 °C. The values of the lattice parameter, i.e., 8.201 and 8.239 Å, obtained in the present study for $LiMn_2O_4$ samples obtained at 800 and 900 °C, respectively, agree with the reported values [32, 33], thus suggesting the formation of the pure phase of $LiMn_2O_4$ by microemulsion route.

The SEM micrographs of the $LiMn_2O_4$ samples prepared at different temperatures are shown in Fig. 3a–f. The particles obtained at 400 and 500 °C appear to be spongy without clear interparticle boundaries. This indicates the poor crystalline nature of these samples. For the samples

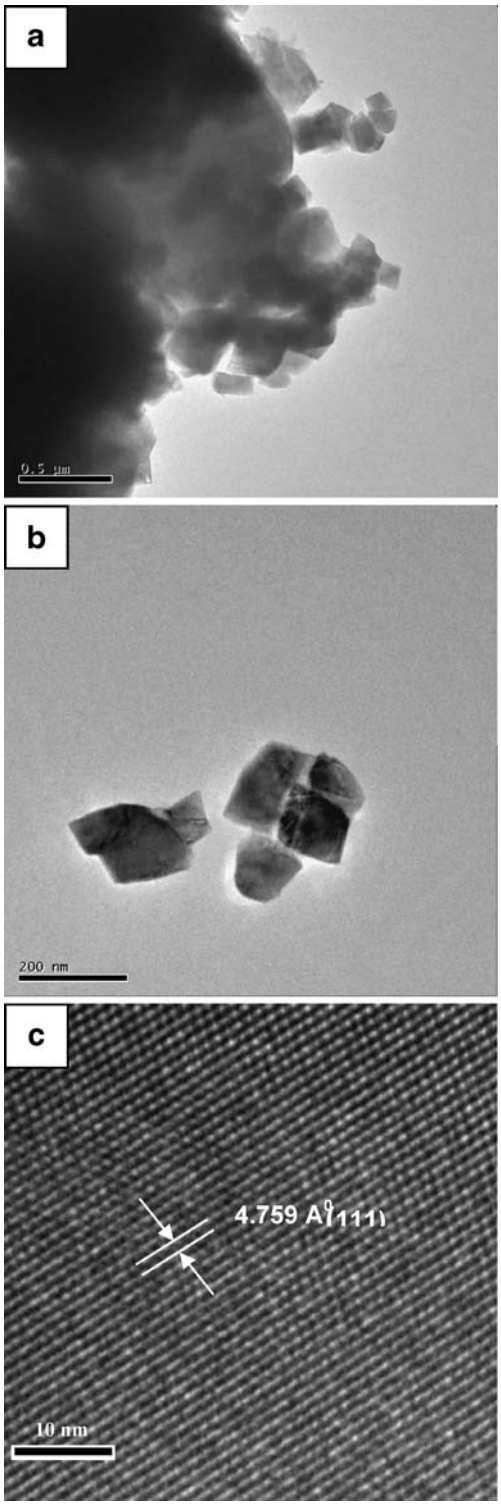

Fig. 4 TEM (**a** and **b**) and HRTEM (**c**) of $LiMn_2O_4$ powder prepared at 900 °C

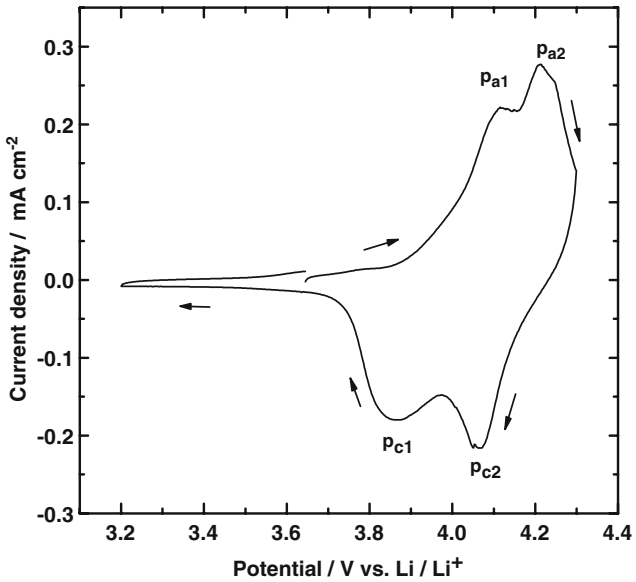

Fig. 5 Cyclic voltammogram of $LiMn_2O_4$ prepared at 900 °C. Sweep rate=0.05 mV s^{-1}. Mass of $LiMn_2O_4$=5 mg cm^{-2}

prepared at a temperature ≥600 °C, clear interparticle boundary is seen, suggesting the good crystalline nature of the samples. The particles are nonspherical in shape with a size of about 200 nm. The EDAX pattern shown in Fig. 3f supports the presence of Mn and O in the sample. The TEM and HRTEM of the sample prepared at 900 °C are presented in Fig. 4. Cubic- or hexagonal-shaped particles of about or less than 200 nm are seen. The HRTEM micrograph (Fig. 4b) exhibits clear lattice fringes with a separation of 4.759 Å. This value corresponds to the (111) plane of the cubic lattice of $LiMn_2O_4$. The particle size of the electrode materials generally employed for battery application is >1 μm. To realize high-rate capabilities of the cells, it is necessary to employ the electrode active materials with smaller particles. With smaller particle size, diffusion path length is smaller and, therefore, the rate of electrochemical process is greater. If nanoparticles are used for enhancing the rate capability, a high reactivity of these nanoparticles with the electrolyte leads to poor cycling performance of the cells. On the other hand, micron-sized particles lead to poor rate capability with long cycle life. Therefore, the particle size between micrometer and nanometer ranges is preferable. The submicron-sized particles of electrode materials are important. The present synthetic method facilitates the formation of submicron-sized particles of $LiMn_2O_4$.

Electrochemical studies

Cyclic voltammogram of an electrode made with $LiMn_2O_4$ heated at 900 °C is shown in Fig. 5. There are two anodic peaks (p_{a1} and p_{a2}) and two cathodic peaks (p_{c1} and p_{c2}) in the potential region between 3.8 and 4.2 V, which are similar to the features of the voltammograms reported in literature [34]. The pair of peaks p_{a1}/p_{c1} correspond to the deintercalation/intercalation of Li in the range $1 \leq x \leq 0.5$ in $Li_xMn_2O_4$, and the p_{a2}/p_{c2} pair correspond to this process of Li in the range $0.5 \leq x \leq 0$ [31]. The p_{a1}/p_{c1} pair is attributed to the removal/addition of Li ions from/into half of the tetrahedral sites in which Li/Li interaction occurs. The p_{a2}/p_{c2} pair is due to this process at the other tetrahedral sites where Li/Li intercalations do not exist [10, 31]. These processes are accompanied by reversible Mn^{3+}/Mn^{4+} redox reactions. These two pairs of current peaks are in good

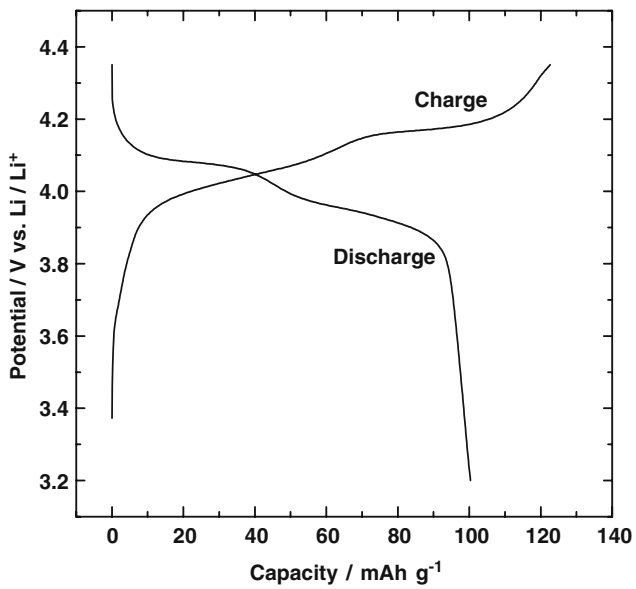

Fig. 6 Charge–discharge curves of $LiMn_2O_4$ electrode at C/5 rate

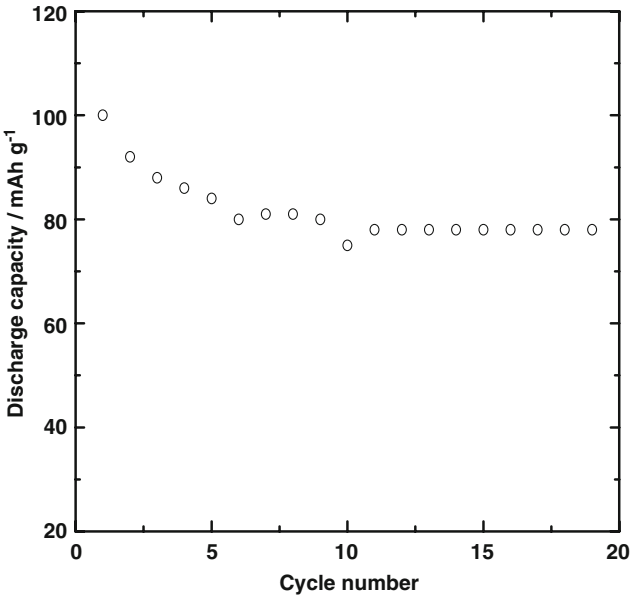

Fig. 7 Variation of discharge capacity of $LiMn_2O_4$ electrode with cycle number at C/5 rate

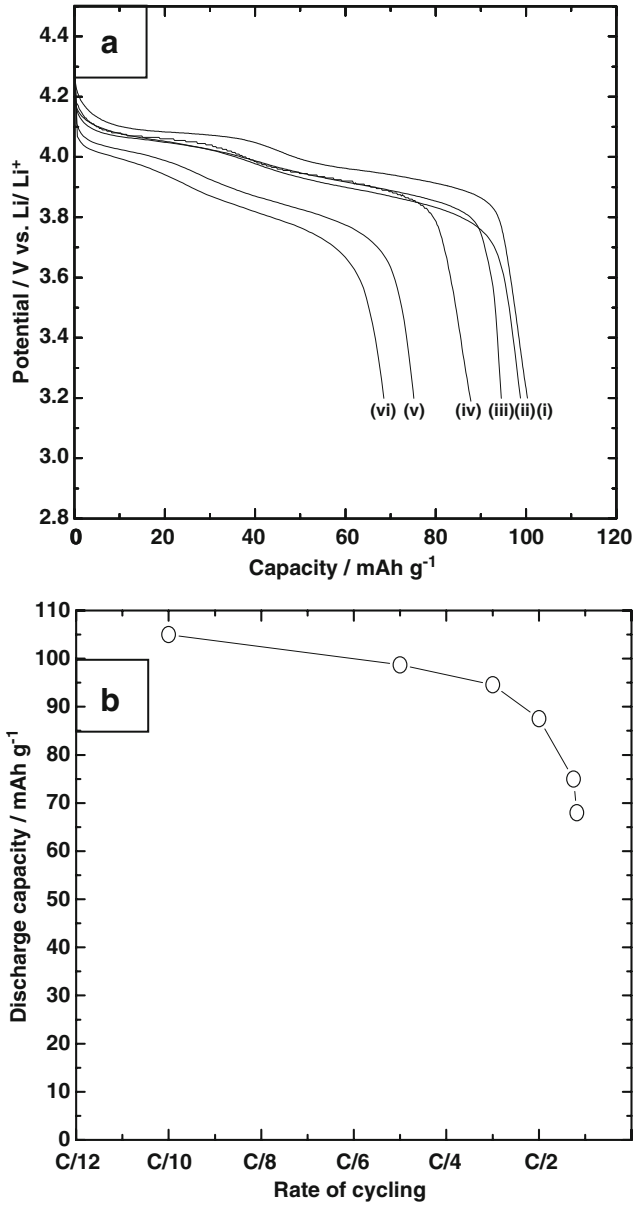

Fig. 8 **a** Discharge curves of $LiMn_2O_4$ electrode at C/10 (*i*), C/5 (*ii*), C/3 (*iii*), C/2 (*iv*), C/1.25 (*v*), and C/0.9 (*vi*) rates. **b** Variation of discharge capacity with rate of cycling

agreement with two different potential plateaus observed during charge–discharge cycling, as described below.

A typical charge–discharge curve of the $LiMn_2O_4$ electrode between 3.2 and 4.3 V is shown in Fig. 6. The variation of potential exhibits two distinct plateaus during both charge and discharge curves (Fig. 6). This type of two-step voltage profile is a characteristic feature of a spinel electrode. The upper potential plateau is attributed to the equilibrium between λ–MnO_2 and $Li_{0.5}Mn_2O_4$, while the lower potential plateau is attributed to the equilibrium between $Li_{0.5}Mn_2O_4$ and $LiMn_2O_4$ [35]. The value of the discharge capacity obtained from Fig. 6 is 100 mAh g^{-1} at C/5 rate and columbic efficiency is close to unity. Although the theoretical capacity of $LiMn_2O_4$ is 148 mA g^{-1}, which corresponds to the complete removal and insertion of Li during charge–discharge cycling, lower values are reported from experimental studies [36–39]. The discharge capacity values depend on the method of preparation of $LiMn_2O_4$ and also on the conditions of charge–discharge cycling. Ahn and Song synthesized $LiMn_2O_4$ by solid-state reaction in the temperature range from 650 to 900 °C, and discharge capacity values between 90 and 100 mAh g^{-1} are reported [36]. A discharge capacity of about 115 mAh g^{-1} at C/5 discharge rate is reported by Lanz et al. for $LiMn_2O_4$ prepared by a ceramic process [37]. In another study, Park et al. reported about 115 mAh g^{-1} at C rate for a commercial sample of $LiMn_2O_4$ powder [38]. For thermally

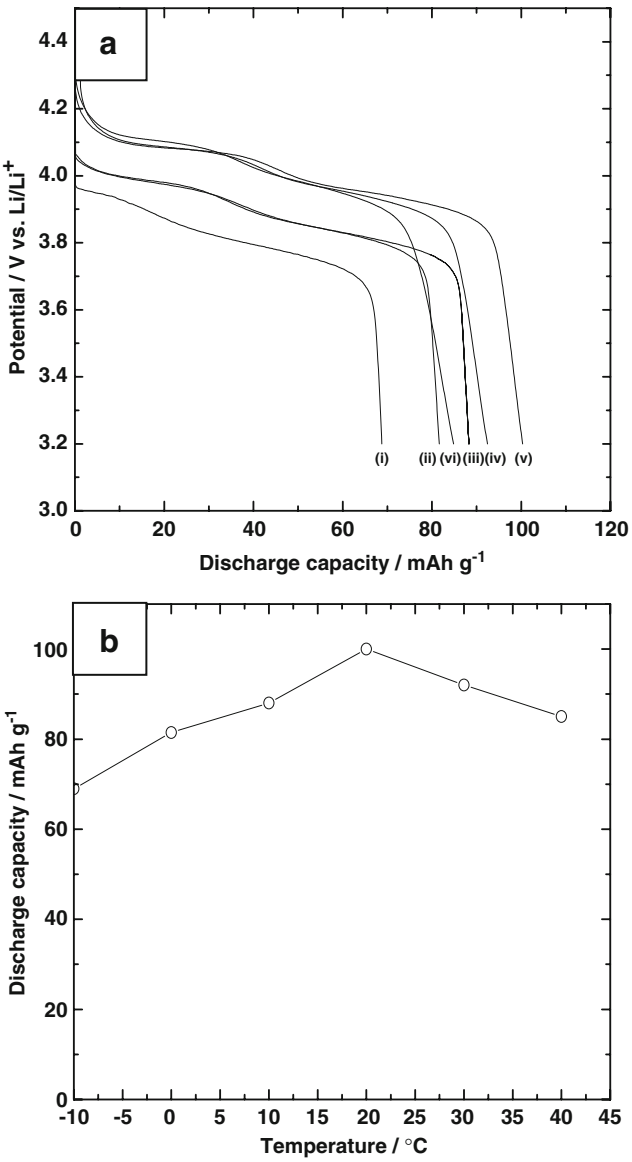

Fig. 9 **a** Discharge curves of $LiMn_2O_4$ electrode at −10 (*i*), 0 (*ii*), 10 (*iii*), 20 (*iv*), 30 (*v*), and 40 °C (*vi*) at C/5 rate. **b** Variation of discharge capacity at C/5 rate with temperature

prepared samples, Lu at al. reported 120 mAh g^{-1} when cycled between 3.5 and 4.5 V [39]. Thus, the discharge capacity 100 mAh g^{-1} obtained in the present work at C/5 rate between 3.2 and 4.3 V (Fig. 6) is comparable with the values reported earlier. The electrode was subjected to charge–discharge cycling, and the discharge capacity against cycle number is shown in Fig. 7. The discharge capacity decreases slightly during the first few cycles and thereafter it stabilizes at 80 mAh g^{-1}. It is known that $LiMn_2O_4$ undergoes a decrease in discharge capacity on repeated charge–discharge cycling due to the dissolution of Mn^{3+} into the electrolyte and also the Jahn–Teller effect associated with Mn^{3+} in the lattice. Decrease in discharge capacity with increasing cycle number is reported previously [36, 39], similar to the results present study (Fig. 7). A $LiMn_2O_4$ electrode was subjected to charge–discharge cycling at different rates, and the discharge curves are shown in Fig. 8a. It is seen that there is a moderate decrease in capacity with an increase of rate of cycling (Fig. 8b).

The effect of temperature on electrochemical properties

The electrochemical properties of $LiMn_2O_4$ heated at 900 °C were evaluated at different temperatures in the range from −10 to 40 °C. Cyclic voltammograms recorded at all temperatures for a $LiMn_2O_4$ electrode were similar to the data shown in Fig. 5 in shape. But peak currents of all four peaks (see Fig. 5) increased with an increase of temperature. Discharge curves recorded at different temperature are shown in Fig. 9a. The potential plateaus reported in Fig. 6a are reproducible at all temperatures. The discharge capacity increased with an increase in temperature up to 20 °C as shown in Fig. 9b due to the enhanced kinetics of the deintercalation/intercalation processes. At a temperature

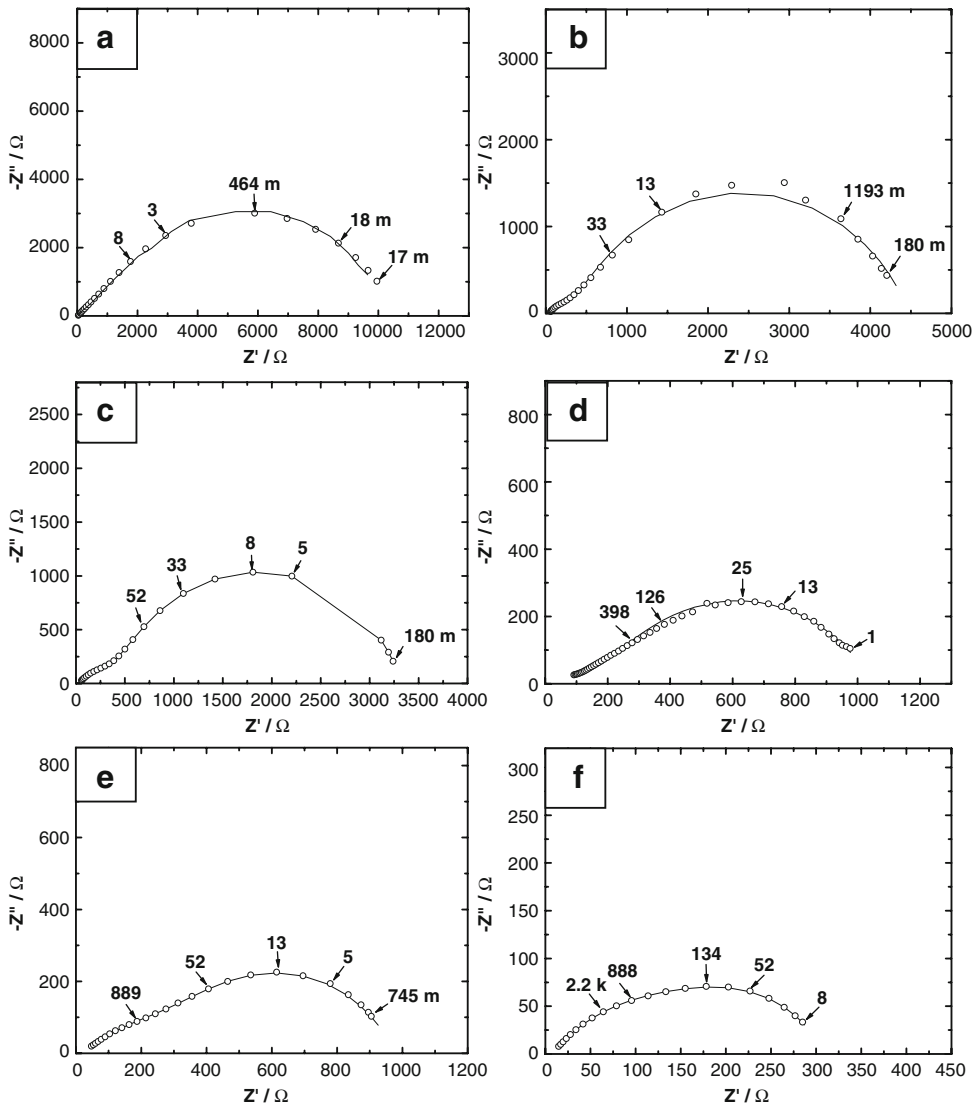

Fig. 10 Nyquist plots of $LiMn_2O_4$ electrode at **a** −10, **b** 0, **c** 10, **d** 20, **e** 30, and **f** 40 °C. Experimental data are shown as *open circles* and theoretical data obtained from fitting are shown as *curves*. Frequency of some data points are given in Hz

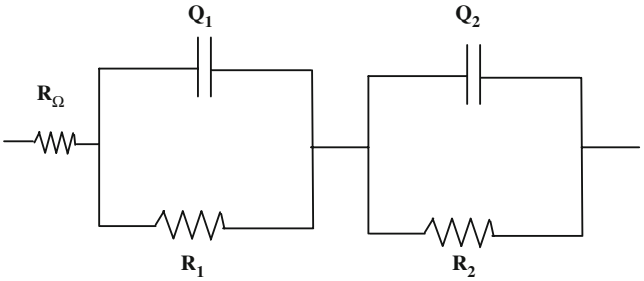

Fig. 11 Equivalent circuit used for NLLS fitting of the experimental impedance data (see text for symbols)

>20 °C, there is a decrease in capacity due to the enhanced dissolution of Mn^{3+} in the electrolyte.

Intercalation/deintercalation of Li in $LiMn_2O_4$ accompanies the Mn^{3+}/Mn^{4+} redox process in solid state within the oxide. Although various aspects of this compound related to crystal structural studies are undertaken and reported in a several reports, electrochemical studies pertaining to the properties of the redox reaction are scarce. $LiMn_2O_4$ prepared in the present study was subjected to ac impedance studies at different temperatures, and the activation energy for the Mn^{3+}/Mn^{4+} redox reaction was evaluated as detailed below. The ac impedance data of a $LiMn_2O_4$//Li cell in discharged condition were measured in the temperature range from −10 to 40 °C, and the Nyquist plots are shown in Fig. 10. Because the area of the Li electrode is larger than that of the $LiMn_2O_4$ electrode and also the Li/Li^+ reaction has high exchange current density, the contribution of the Li electrode toward the measured impedance is likely to be negligibly small. To justify this assumption, a symmetrical Li//Li cell was assembled in addition to a $LiMn_2O_4$//Li cell, and their impedances were compared. The diameter of the semicircle of the Li//Li symmetrical cell was only about 5 Ω, whereas it is more than 1,000 Ω for the $LiMn_2O_4$//Li cell at ambient temperature. Hence, the measured cell impedance is considered equal to the impedance of the $LiMn_2O_4$ electrode. The data shown in Fig. 10 were measured at the required temperature after the electrode was discharged to 3.2 V followed by rest of the cell for 3 h. The Nyquist plot at each temperature consists of a high-frequency intercept and a broad semicircle. A few data points, which corresponded to a linear segment at the lower frequency region than the semicircle region, were deleted for the purpose of fitting the rest of the data to an equivalent circuit as detailed below. The broad semicircle is due to the overlap of two semicircles. The impedance parameters were evaluated by fitting the data to an equivalent circuit using a nonlinear least squares (NLLS) fitting program [40]. The suitable equivalent circuit, which was found to fit the impedance data, is shown in Fig. 11. The resistance R_Ω represents the ohmic resistance, which includes the resistance of the electrolyte, current collectors, electrical leads, etc. The two semicircles (Fig. 10) of each Nyquist plot are due to two pairs of parallel resistance and capacitances [41]. Because the semicircles are depressed with their centers below the real axis, capacitors are replaced by constant phase element (CPE, Q) in Fig. 11 [42]. Accordingly, R_1 and Q_1 are the resistance and CPE, respectively, corresponding to the high-frequency semicircle, and R_2 and Q_2 are the resistance and CPE, respectively, corresponding to the low-frequency semicircle. CPE (Q) is mathematically defined in admittance as:

$$Q = Q^0(j\omega)^n \tag{1}$$

where Q^0 is an adjustable parameter, ω is an angular frequency, and n is a constant. If n=1, CPE represents a capacitance (C) with Q^0=C. Similar to the data of the $LiMn_2O_4$ electrode obtained in the present study, the impedance of $LiCoO_2$ was shown to consist of two semicircles [43]. It was concluded that the formation of a surface layer on the $LiCoO_2$ was responsible for the high-frequency semicircle and the kinetics of intercalation/deintercalation of Li in the electrode for the low-frequency semicircle. Accordingly, R_1 is the resistance of the surface film on $LiMn_2O_4$ and Q_1 is the CPE corresponding to the surface film capacitance. The impedance parameters R_2 and Q_2 are the resistance and CPE, respectively, corresponding to the electrochemical intercalation/deintercalation process and double-layer capacitance. The impedance parameters were obtained by fitting the data (Fig. 10) to the equivalent circuit (Fig. 11). The resistance R_2 corresponds to the intercalation/deintercalation of Li^+ at the $LiMn_2O_4$ electrodes and it is equivalent to charge-transfer resistance (R_{ct}=R_2) of the electrochemical process, namely, Mn^{3+}/Mn^{4+} redox process.

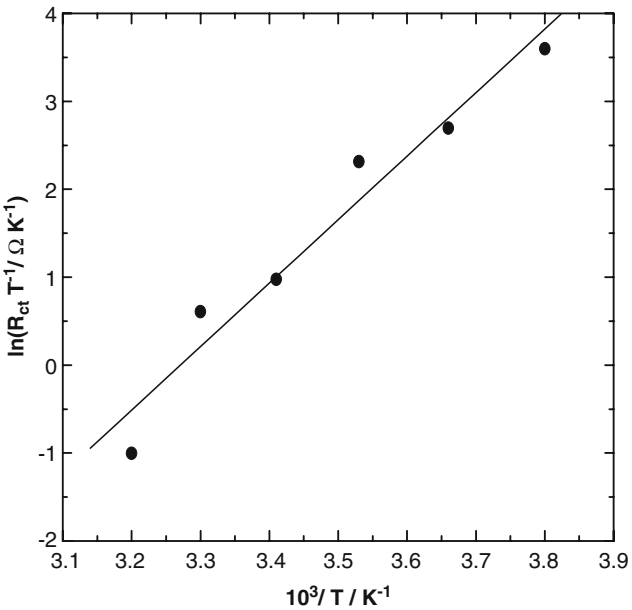

Fig. 12 Plot of ln (R_{ct}/T) against inverse of temperature (T)

R_{ct} is related to the exchange current density (I_o) of the reaction by Eq. 2 [44]:

$$R_{ct} = RT/(FI_o) \quad (2)$$

where R is the gas constant, T is the absolute temperature, and F is the Faraday constant. By suitable substitution of I_o by the rate constant and state-of-charge of the electrode, it is possible to arrive at Eq. 3 [45]:

$$R_{ct} = \frac{KT \exp(E_a/RT)}{S^{\alpha}} \quad (3)$$

where K is a constant, E_a is the activation energy, S is the state-of-charge, and α is the transfer coefficient of the reaction. From Eq. 2, we get Eq. 4:

$$\frac{d \ln (R_{ct}/T) E_a}{d(1/T)} = \frac{E_a}{R}. \quad (4)$$

Thus, it is possible to evaluate the activation energy (E_a) of the reaction. The values of R_{ct} (=R_2; obtained from fitting the impedance data) were used to plot ln (R_{ct}/T) against $1/T$ as shown in Fig. 12. The plot is fairly linear. From the slope of this plot, 0.62 eV is obtained for E_a. It may be noted that the impedance data were measured when the $LiMn_2O_4$ electrode was in discharged condition, and therefore, this value of E_a corresponds to the Mn^{3+}/Mn^{4+} redox process in the discharged state of the electrode. Thus, the temperature-dependent impedance measurements provide an important electrochemical property, namely, activation energy associated with change in oxidation state of Mn in $LiMn_2O_4$. The extension of these studies to other lithium transition metal oxides is in progress in our laboratory.

Conclusions

Submicron-sized particles of the $LiMn_2O_4$ spinel are synthesized via microemulsion route. The precursor powder exhibits pure crystalline spinel structure by annealing at 900 °C. Electrochemical characterization studies provide a discharge capacity of 100 mAh g^{-1} at C/5 rate, and there is moderate decrease in capacity by increasing the rate of charge–discharge cycling. From electrochemical impedance measurements conducted at different temperatures, the value of the activation energy obtained for the Mn^{3+}/Mn^{4+} redox process accompanying the intercalation/deintercalation of Li^+ at $LiMn_2O_4$ is 0.62 eV.

References

1. Nazri GA, Pistoia G (2004) Lithium batteries: science and technology. Kluwer, Boston, p 1
2. Whittingham MS (2004) Chem Rev 104:4271
3. Ammunsdsen B, Paulsen J (2001) Adv Mater 13:943
4. Zhang Y, Shin HC, Dong J, Liu M (2004) Solid State Ionics 171:25
5. Tarascon JM, Gurgeon S, Morcrette M, Laruelle S, Rozier P, Poizot P (2005) C R Chimie 8:9
6. Jiang Z, Abraham M (1996) J Electrochem Soc 143:1591
7. Raimondi F, Scherer GG, Kotz R, Wokaun A (2005) Angew Chem 44:2190
8. Petri OA, Tsirlina GA (2001) Russ Chem Rev 70:285
9. Jamnik J, Maier J (2003) Phys Chem Chem Phys 5:5215
10. Hwang BJ, Santhanam R, Liu DG (2001) J Power Sources 97/98:443
11. Hon YM, Fung KZ, Lin SP, Hon MH (2001) J Ceram Soc Jpn 109:986
12. Hon YM, Lin SP, Fung KZ, Hon MH (2002) J Eur Ceram Soc 22:653
13. Lu CH, Lin Y, Wang HC (2003) J Mater Sci Lett 22:615
14. Curtis CJ, Wang J, Schulz DL (2004) J Electrochem Soc 151:A590
15. Tsuji T, Tatsuyama Y, Tsuji M, Ishida K, Okada S, Yamaki J (2007) Mater Lett 61:2062
16. Cabana J, Valdes-soils T, Palacin MR, Ore-Sole J, Fuertes A, Marban G, Fuertes AB (2007) J Power Sources 166:492
17. Li X, Cheng F, Guo B, Chen J (2005) J Phys Chem B 109:14017
18. Sides CR, Li N, Patrissi C, Charles J, Scrosati B, Martin CR (2002) MRS Bull 27:604
19. Subramania A, Angayarkanni N, Vasudevan T (2007) Mater Chem Phys 102:19
20. Wu HM, Tu JP, Yang YZ, Shi DQ (2006) J Mater Sci 41:4247
21. Taniguchi I, Bakenov Z (2005) Powder Technol 159:55
22. Son JT, Kim HG, Park YJ (2004) Electrochim Acta 50:453
23. Vivkanandhan S, Venkateswarlu M, Satyanarayana N, Suresh P, Nagaraju DH, Munichandraiah N (2006) Mater Lett 60:3212
24. Si P, Bian X, Liu Y, Li H, Zhang Y (2003) J Mater Sci Technol 11:50
25. Lopez-Quintela MA (2003) Curr Opin Colloid Interface Sci 8:137
26. Hwang KT, Um WS, Lee HS, Song JK, Chung KW (1998) J Power Sources 74:169
27. Myung ST, Chung HT (1999) J Power Sources 84:2
28. Lu CH, Lin SW (2001) J Power Sources 93:14
29. Lu CH, Saha SK (2001) J Mater Sci Lett 20:1841
30. Cushing BL, Kolesnichenko VL, O'Connor CJ (2004) Chem Rev 104:3893
31. Xia Y, Yoshio M (1996) J Electrochem Soc 143:825
32. Naghash AR, Lee JY (2000) J Power Sources 85:284
33. Han YS, Kim HG (2000) J Power Sources 88:161
34. Shen P, Jia D, Huang Y, Liu L, Guo Z (2006) J Power Sources 158:608
35. Lu CH, Lin Y (2003) J Mater Res 18:552
36. Ahn DS, Song MY (2000) J Electrochem Soc 147:874
37. Lanz M, Kormann C, Steninger H, Heil G, Hass O, Noavak P (2000) J Electrochem Soc 147:3997
38. Park SC, Kim YM, Kang YM, Kim KT, Lee PS, Lee JY (2001) J Power Sources 103:86
39. Liu Z, Yu A, Lee JY (1998) J Power Sources 74:228
40. Boukamp BA (1989) Equivalent circuit: users manual. University of Twente, The Netherlands, p 1
41. Roudrigues S, Munichandraiah N, Shukla AK (2000) J Power Sources 87:12
42. Macdonald JR (1987) Impedance spectroscopy. Wiley, New York, p 1
43. Thomas MGSR, Bruce PG, Goodenough JB (1985) J Electrochem Soc 132:1521
44. Bard AJ, Faulkner LR (1980) Electrochemical methods. Wiley, New York, p 105
45. Suresh P, Shukla AK, Munichandraiah N (2002) J Appl Electrochem 32:267